Carbon 130 (2018) 680–691

Contents lists available at ScienceDirect

Carbon

journal homepage: www.elsevier.com/locate/carbon

Carbon materials with hierarchical porosity: Effect of template removal strategy and study on their electrochemical properties

Xiaowei Liu [a], Xuehua Liu [a], Baofen Sun [a], Heliang Zhou [a], Aiping Fu [a], Yiqian Wang [b], Yu-Guo Guo [a, c], Peizhi Guo [a], Hongliang Li [a, *]

[a] Institute of Materials for Energy and Environment, Laboratory of New Fiber Materials and Modern Textile, Growing Basis for State Key Laboratory, College of Materials Science and Engineering, Qingdao University, Qingdao 266071, China
[b] College of Physics, Qingdao University, No. 308 Ningxia Road, Qingdao, 266071, China
[c] Beijing National Laboratory for Molecular Sciences, Institute of Chemistry, Chinese Academy of Sciences (CAS), Beijing 100190, China

ARTICLE INFO

Article history:
Received 10 October 2017
Received in revised form
10 January 2018
Accepted 11 January 2018
Available online 12 January 2018

ABSTRACT

The porosity of carbon materials can be tuned by controlling the template removal strategies in silica/carbon composites. In this study, chitosan was used as precursor for carbon, and SiO_2 nanoparticles were selected as the template for mesopores. The spray drying technique was adopted for the fabrication of silica/chitosan microspheres. Porous carbon with hierarchical macro/meso/micro pores was obtained through a facile one-pot high temperature treatment, in which the pyrolysis of the chitosan precursor, removal of the silica template, and introduction of macropores coordinatively occur using PTFE (polytetrafluoroethylene) binder as a silica etchant and also as a macropore director. This approach not only simplifies the fabrication processes but also yields regular honeycomb-like carbon with macro/meso/micro-sized hierarchical pore structure with high specific surface areas up to 1011 $m^2 g^{-1}$. A supercapacitor assembled with porous carbon as the electrode exhibited a high specific capacitance of 250.5 $F g^{-1}$ at a current density of 0.5 $A g^{-1}$ using 6 mol L^{-1} KOH as the electrolyte in a three-electrode system. The supercapacitor also delivered excellent cycling stability with an enhancement of capacity up to 107% over 5000 cycles at a high current density of 10 $A g^{-1}$.

1. Introduction

The rapid growth in energy demand has prompted researchers to find new materials with which to develop efficient energy storage devices. In energy storage systems of the past few decades, supercapacitors or electrochemical capacitors have caused great concerns due to their rapid charge and discharge characteristics, such as high power density and excellent cycle stability [1–5]. According to the energy storage mechanism, electrochemical capacitors are generally classified into two categories – electrochemical double-layer capacitors (EDLCs) and pseudo capacitors [6]. The charge storage of EDLCs mainly depends on the physical adsorption and desorption of ions at the interface of the electrode and electrolyte, while pseudocapacitors store charges via chemical faradaic redox reactions through electroactive groups on the surface of the electrode [7]. Among various available materials, carbonaceous materials, such as porous carbon [8,9] and graphene [10], have been widely used in the manufacture of supercapacitors because of their large specific surface area, high electrical conductivity, excellent physicochemical stability, and low cost. The capacitance of EDLCs is generated from the charge accumulation at the electrode and electrolyte interface [11–13]. Therefore, the surface area of carbon-based electrodes is the key concern for application of EDLCs. However, even with a large specific surface area, the capacity is still relatively low due to the irregular pore structure, which impedes ion motion. In comparison with disordered porous materials, hierarchically porous carbon (HPC) with ordered pore architecture and connected pore channels can shorten the ion diffusion pathways. This type of pore structure will reduce the resistance of molecular movement and hence make it easier for ions to diffuse in microsized pores [14].

Recently, a series of methods have been applied for the preparation of hierarchically porous carbon. They can mainly be divided into two main approaches, i.e., (1) using a template to introduce

* Corresponding author.
E-mail address: lhl@qdu.edu.cn (H. Li).

https://doi.org/10.1016/j.carbon.2018.01.046
0008-6223/

pores followed by a chemical activation, and (2) physical supplementary methods [15]. Although various template-free strategies to synthesize HPC have been published as alternative approaches, these processes involve large amounts of surfactants [16]; expensive precursors such as imide, dopamine, and phenol; and complicated self-formation processes with organic solvents, for example, dimethyl imidazole or trimesic acid [17–19]. Among these techniques, the most commonly used strategy for preparation of HPC is a combination of two or more of the methods mentioned above, which typically involve separated two-step processes consisting of the introduction of macro- or meso-sized pores and subsequent chemical activation. Taking into consideration the lengthy activation process of surfactant-directed methods and the inability to precisely control the pore size of the non-templating methods, the hard template strategy utilizing different types of particles, such as silica [20], metal oxide [21–23], and molten salt [24,25], would be an efficient method to obtain porous carbon with a desirable structure. As a type of hard template, silica exhibits several virtues, such as facile morphology and particle size controllability, good uniformity, and high dispersity [26]. However, there are few reports regarding the preparation of porous structure with hierarchical micro/meso/macro pores using only one batch of silica as the template [27–29], because the introduction and the subsequent removal of macrosized template could lead to severe destruction of the integrality of the as-prepared hierarchical porous structure. Thus, a facile approach for removing silica and simultaneously introducing macro-, meso-, and microsized pores is desirable for producing HPCs with hierarchical porosity and high specific surface area.

Herein, we report on the preparation of honeycomb-like porous carbon with micro-, meso-, and macrosized hierarchical pores by a one-pot template removal and carbonization coordinated process. In the preparation, chitosan was used as the carbon precursor, and nanosized SiO_2 particles were chosen as a hard template for mesopores. PTFE (polytetrafluoroethylene) binder was utilized as a silica removal agent, and it also acts as a template for directing macropores. The mechanism of silica template etching by PTFE and its influences on the pore size of porous carbon were investigated. The obtained carbon materials exhibited unique regular porous structures with outstanding electrochemical performance when they were used as electrode materials for supercapacitors in aqueous electrolyte and organic electrolyte. For porosity control studies, two other types of template removal approaches, such as high temperature corrosion with PTFE powder and wet solution etching by hydrofluoride (HF), have also been investigated. The regulation of the three different template removal processes was compared, and the electrochemical properties of the carbon materials derived from the corresponding etching methods were studied in detail.

2. Experimental section

2.1. Materials

Chitosan, isopropyl alcohol, N-methy-l-pyrrolidone, potassium hydroxide and hydrofluoride acid were purchased from Sino Reagent Co., Ltd. 30 wt% LUDOX® LS colloidal SiO_2 with size of about 12 nm and fume silica powder with size of about 14 nm were purchased from Sigma-Aldrich (Shanghai) Trading Co., Ltd. The separator, $LiPF_6$, PTFE (polytetrafluoroethylene) powders, PTFE binder suspension (60 wt%), acetylene black and nickel foam were used as purchased. All chemicals were analytical grade and used without further purification. Deionized water was employed throughout the experiments.

2.2. Preparation of silica/chitosan microspheres

The silica/chitosan microspheres were prepared via a spray-drying-assisted method. A laboratory-scale SP-1500 spray dryer was utilized for the spray-drying process (Shanghai SunYi Tech Co., Ltd.). In a typical batch, 2 g of chitosan was dissolved in 100 mL of 5 wt% acetic acid aqueous solution, and then 4 mL of colloidal Ludox SiO_2 was added to the chitosan solution, followed by a 12 h agitation until a transparent suspension was obtained. Then, the suspension was dried by the spray dryer at 180 °C with hot air as the carrier gas. The silica/chitosan composite spheres were collected by a cyclone separator connected to the spray dryer. The amount of silica in the silica/chitosan composites was determined to be 60 wt % using thermogravimetric analyses conducted under an air atmosphere (Fig. S1).

2.3. Preparation of porous carbon with different porosities

The as-prepared silica/chitosan composites and PTFE binder suspension with a weight ratio of 1:2 were dispersed in 20 ml of deionized water, followed by freeze drying for 24 h. Then, the dried solid mixture was thermally treated in a tube furnace at 900 °C for 4 h under a flow of high-purity argon gas. After cooling to room temperature, black powder was collected and denoted as the PBE (PTFE binder etched) sample. The silica/chitosan composites were also blended with PTFE powder at the same weight ratio, followed by the same thermal treatment as applied to PBE. Finally, black powder was obtained and was designated as the PPE (PTFE powder etched) sample. As control experiments, the aforementioned mixtures of silica/chitosan spheres and PTFE were thermally treated at different temperature intervals, e.g., 350 °C and 500 °C, to investigate the status of the intermediates. The traditional etching method with HF aqueous solution was also utilized. Firstly, the as-prepared silica/chitosan composites were carbonized in a tube furnace at 900 °C for 4 h under a flow of high-purity argon gas. Then, the silica/carbon spheres derived from the thermal treatment were dispersed into a 20% HF aqueous solution for 24 h at ambient temperature to remove the silica by etching. The black solid was collected by centrifugation and washed with deionized water and ethanol several times, and then, the solid was dried at 70 °C in air for 24 h and was denoted as the HE (HF etched) sample.

2.4. Characterization

The crystallographic information and composition of the products were investigated using a Rigaku Ultima IV X-ray diffractometer (XRD, Cu-Kα radiation $\lambda = 0.15418$ nm). Raman spectra were collected using a Renishaw inVia Plus Micro-Raman spectroscopy system equipped with a 50 mW DPSS laser at 532 nm. The specific surface areas were estimated with the Brunauer-Emmett-Teller (BET) method with N_2 adsorption data in the relative pressure range of $P/P_0 = 0.05–0.35$. The pore size distributions were calculated using the Barrett-Joyner-Halenda (BJH) model applied to the desorption branch of the N_2 isotherms obtained with a Quantachrome Autosorb-IQ-MP/XR surface area and pore analyzer. The thermogravimetric analysis was performed with a Mettler Toledo TGA-2 thermal gravimetric analyzer under an oxygen atmosphere with a heating rate of 10 °C min^{-1}. The morphologies and the structures of the samples were examined by a JEOL JSM-7800F scanning electron microscope (SEM) and a JEOL JEM-2100 transmission electron microscope (TEM).

2.5. Electrochemical measurement

The electrochemical measurements were conducted using a

three-electrode configuration in 6 M KOH electrolyte with platinum foil as the counter electrode and Hg/HgO as the reference electrode. The working electrodes were prepared by mechanically mixing 85 wt% powdered porous carbon, 5 wt% acetylene black, and 10 wt% PTFE binder in isopropyl alcohol to form a slurry. Then, the homogenous slurry was pressed onto a 1 cm^2 nickel foam current collector and finally dried in a vacuum at 110 °C for 10 h. The mass loading of active material on the electrode was 1–2.5 mg. All electrochemical tests were performed using an electrochemical workstation (Chenhua CHI760D) at room temperature. The gravimetric specific capacitance was calculated from the galvanostatic charge-discharge curves by the following equation:

$$C = I^*\Delta t/m^*\Delta V \quad (1)$$

To fabricate the PBE//PBE symmetrical supercapacitor and study its electrochemical properties in organic electrolyte, electrodes were prepared by mixing the obtained PBE samples, acetylene black, and PVDF (Polyvinylidene Fluoride) binder with a mass ratio of 80:10:10 in N-methy-l-pyrrolidone, which was then ground with an agate mortar to form a homogeneous slurry. The slurry mixture was pasted onto a piece of aluminum foil. After drying under vacuum at 110 °C for 10 h, the aluminum foil with active materials was cut into disks of 1-cm diameter and then weighed. 2 mg of active material was loaded on each electrode. The symmetrical electrodes were assembled using a 1 M solution of $LiPF_6$ in EC: DEC: DMC with a volume ratio of 1:1:1 (Tianjin Jinniu Power Sources Material Co., LTD) as the electrolyte and Celgard 2400 film as the separator in CR2032 stainless steel coin-type cells. The cyclic voltammetry (CV) and galvanostatic charge/discharge (GCD) tests in two electrode cells were performed at a potential window of 0–3 V. The specific capacitance of the material was calculated from Equation (2), and the energy density E (Wh kg^{-1}) and power density P (W kg^{-1}) were calculated from Equations (3) and (4), respectively,

$$C = 4I \times \Delta t/(m \times \Delta V) \quad (2)$$

$$E = C \times \Delta V^2/(2 \times 4 \times 3.6) \quad (3)$$

$$P = 3600 \times E/\Delta t. \quad (4)$$

where C (Fg^{-1}) represents the specific capacitance, I (A) represents the discharge current, Δt (s) corresponds to the discharge time, ΔV (V) represents the potential change within Δt, and m (g) represents the loading mass of the active material in each electrode.

3. Results and discussion

3.1. Morphology and structure

The morphologies of the porous carbon before and after silica etching were observed by scanning electron microscopy (SEM). From the SEM images, one can see that all the silica/chitosan composites show a spherical but creased morphology with a diameter of approximately 2 μm (Fig. 1a), which can be attributed to the inhomogeneous shrinkage induced by the instantaneous drying effect during the spray drying process. For the HE and PPE samples, there is no obvious alteration in morphology after carbonization and the template etching process; however, their sizes slightly decreased in comparison with the silica/chitosan spheres (Fig. 1b and c). Such a change can be ascribed to the shrinkage effect during the carbonization process. No obvious macropores can be observed in them, but their surfaces became slightly rough after the removal of silica due to the formation of abundant mesosized pores (Fig. 1h and g). From Fig. 1d and e, one can see that PBE possesses abundant macrosized pores with a mean size of approximately 200 nm, which can be ascribed to the anchoring of the rod-like PTFE nanoparticles on the surface of the silica/chitosan spheres and the *in-situ* decomposition therein. In addition, a large number of mesopores can be observed in the depths of the macropores, suggesting the hierarchical macro-meso porous structure (Fig. 1f). Control experiments show that superfluous PTFE, e.g., with a ratio of 1:4 between silica/chitosan composites and PTFE binder, will destroy the integrality of these macropores, while an insufficient weight ratio (1:1) will not completely etch silica (Fig. S2). The deterioration of the macrostructure or the silica residue in the structure will lead to poor electrochemical performances when the samples are utilized as electrode material for supercapacitors (please refer to Fig. S11). In contrast, the carbon materials with an integrated hierarchical porous structure will facilitate quick transportation of ions and improve ionic conduction (see section 3.5 Electrochemical properties).

To elucidate the structure in detail, these samples were further characterized by transmission electron microscopy (TEM). The TEM images also indicate that HE (Fig. 2a and d) and PPE (Fig. 2b and e) possess a spherical morphology and contain abundant mesosized pores with a diameter of approximately 10 nm. However, the ordering of the pores in all three samples is low. Such a disordered characteristic of the resultant mesopores that occurred from the use of SiO_2 as a template is reasonable because the SiO_2 particles are randomly dispersed inside the SiO_2/chitosan spheres as well as the corresponding SiO_2/carbon composites. However, the low resolution TEM image of PBE shows a high density of wormhole-like macropores with sizes of approximately 200 nm (Fig. 2c). Interestingly, it can be found from the high magnification image that the walls of the macropores possess numerous mesosized pores with diameters of approximately several nanometers (Fig. 2f), presenting perfect hierarchical pore structures in PBEs. In addition, some mesopores have been observed that appear unusual, and these are marked in the high resolution TEM micrograph (Fig. 2f). The exception might be ascribed to the overcorrosion of the carbon sheet by PTFE or the aggregation of nanosized silica templates inside the composite carbon spheres, which then leads to the collapse of the mesopores after etching.

3.2. Thermal stability and composition

Fig. 3a depicts the thermogravimetric analysis (TGA) curves of these three different porous carbon materials tested between room temperature and 800 °C. The slight weight loss below 100 °C is attributed to the removal of adsorbed water, while the sharp weight loss at approximately 450 °C corresponds to the removal of residual oxygen groups on carbon spheres and the subsequent burning of carbon skeleton. The residues of approximately 5.6 wt%, 8.0 wt%, and 3.4 wt% for PBE, PPE, and HE, respectively, were determined from the TGA data. Energy dispersive spectroscopy (EDS) measurements were also performed in conjunction with a SEM, and the percentages obtained of Si in PBE, PPE, and HE were 0.64 wt%, 0.8 wt%, and 0.81 wt%, respectively. The SiO_2 content derived from the EDS technique is much lower than that obtained by the TGA method. Normally, both energy dispersive X-ray (EDX) analysis and X-ray photoelectron spectroscopy (XPS) techniques are surface- and area-sensitive methods, whereas TGA can detect all the nonvolatile materials in the bulk. Thus, our experimental results obtained by TGA are more reliable. Compositional analysis of the sample surface was carried out using XPS (Fig. 3b). Characteristic peaks for C1s, O1s, and N1s were observed for all these samples in their XPS full surveys. However, additional peaks for Si2s and Si2p corresponding chemical environments, i.e., Si-O, were

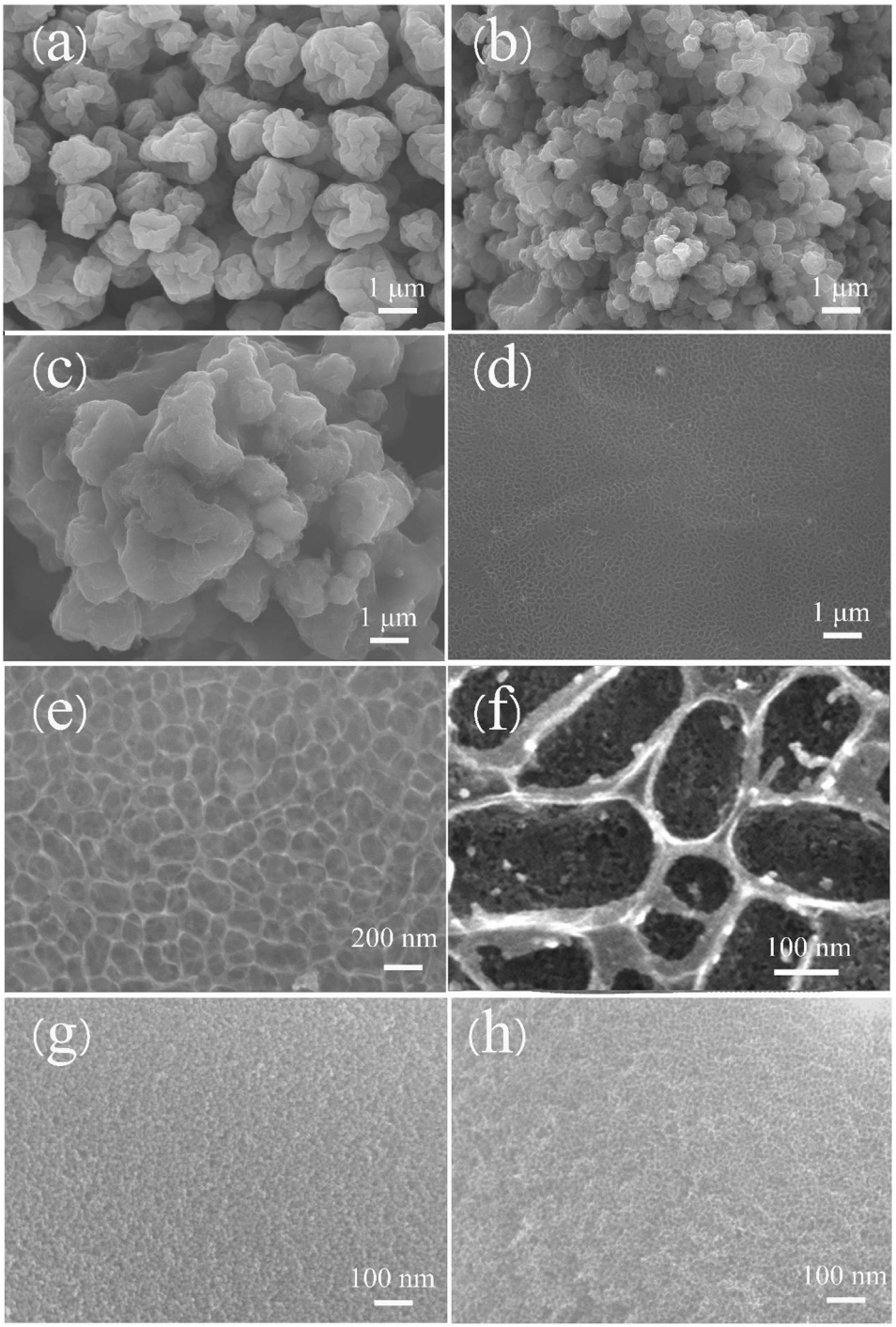

Fig. 1. SEM images of silica/chitosan composites (a), HE (b), PPE (c), PBE (d) and (e), and magnified SEM images of PBE (f), PPE (g) and HE (h).

detected for HE. Table 1 shows a nitrogen content of 1.64, 1.35, and 0.8 at.% for PBE, PPE, and HE, respectively, which were calculated based on the characteristic peaks of N. The high content of oxygen and the presence of Si^{4+} (Fig. 3f) reveal the presence of silica on the surface of HE. Actually, the SiF_4 species derived from the reaction between the silica template and HF will diffuse out of the pores and hydrolyze again due to the concentration variation, and the reformed SiO_2 can then be deposited onto the external surface of the resultant carbon spheres [30]. The silica adsorbed on the surface may hinder the oxidation of carbon in air and hence lead to a 90 °C enhancement of decomposition temperature for HE (Please refer to Fig. 3a). Additionally, the relative content of nitrogen decreased with the deposition of silica on the surface. To further investigate the valence state of nitrogen, high resolution XPS surveys at the N1s region were conducted and are presented in Fig. 3 as panels c, d, and e. All these spectra can be deconvoluted into three peaks at 402.5 ± 0.3, 400.07 ± 0.3, and 398.01 ± 0.3 eV, corresponding to quaternary (N-X), pyrrolic/pyridine (N-5), and pyridinic (N-6) nitrogen, respectively [31,32].

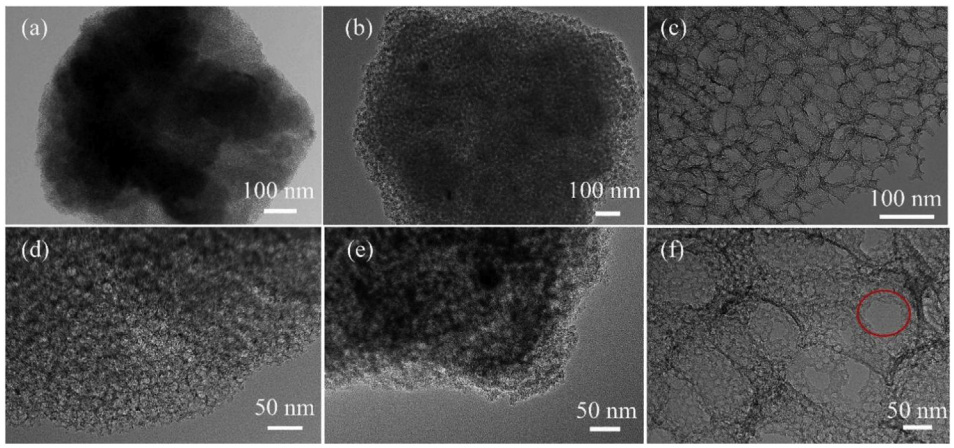

Fig. 2. TEM images of (a) HE; (b) PPE; (c) PBE; and HRTEM images of (d) HE; (e) PPE; (f) PBE. (A colour version of this figure can be viewed online.)

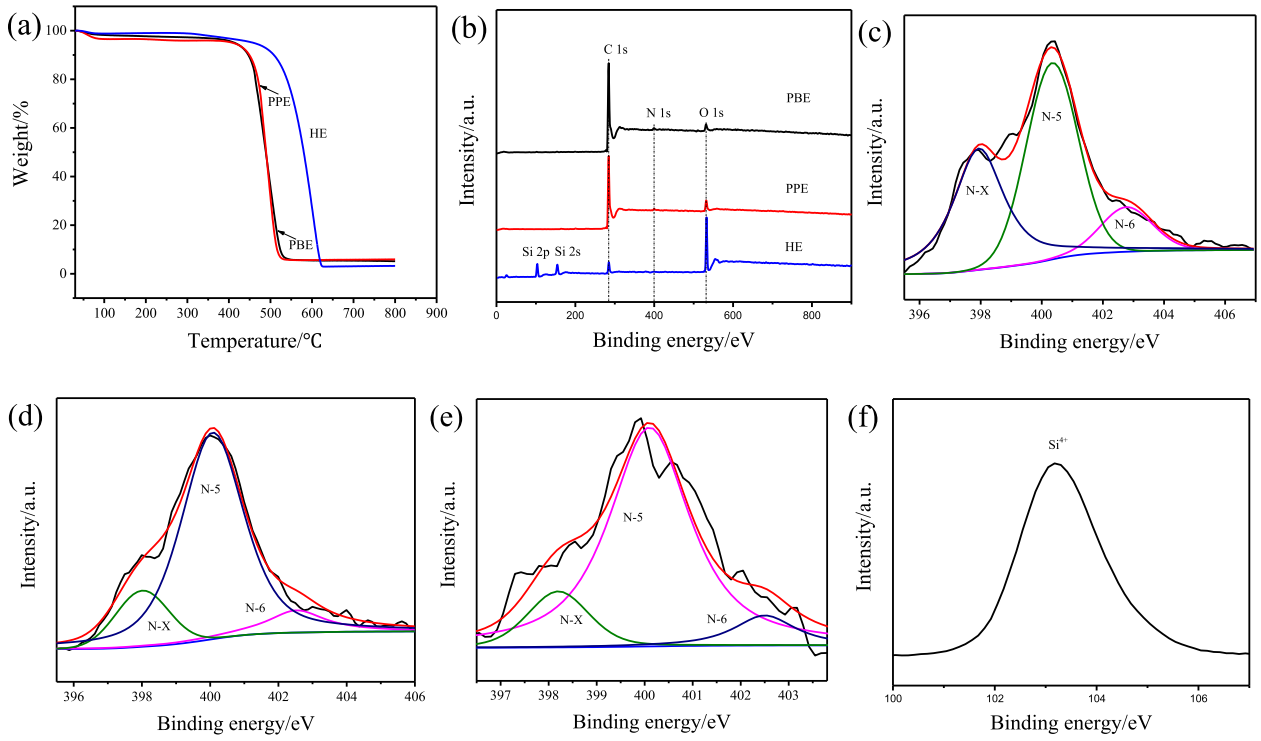

Fig. 3. TGA curves (a) and XPS surveys (b) of these samples, high-resolution XPS surveys for PBE (c), PPE (d) and HE (e) at N1s region, and high-resolution XPS survey of Si2p for HE (f). (A colour version of this figure can be viewed online.)

Table 1
XPS analysis of as-prepared samples.

Sample	C/at. %	O/at. %	N/at. %	Si/at. %
PBE	95.03	3.33	1.64	/
PPE	93.2	5.45	1.35	/
HE	25.67	50.6	0.8	22.93

3.3. Phase and porosity

XRD patterns are illustrated in Fig. 4a. There are two broad but very weak diffraction peaks centered at approximately 22.7° and 42.5° that correspond to the (002) and (100) planes of graphite, respectively. In comparison with pristine graphite, the (002) peak for these porous carbon materials shifted to the low angle direction, which suggests the presence of amorphous characteristics. Similarly, the intensity of the (100) peak fades and the position gradually shifts to the lower angle direction from HE to PBE. Such phenomena can occur because of the existence of micropores and defects in these carbon materials, which result in the deterioration of their graphitization [33], and such speculation has been confirmed by Raman spectra tests and N_2 adsorption-desorption measurements. As shown in Fig. 4b, two Raman bands corresponding to disorder D band (1345 cm^{-1}) and sp^2-hybridized G band (1600 cm^{-1}) have been detected for all the samples. The ratio of the relative intensities of D band and G band (I_D/I_G) can be used to estimate the graphitic degree of carbon materials [34,35]. The I_D/I_G for HE, PPE, and PBE was determined to be 0.86, 0.88, and 0.91, respectively. The high I_D/I_G of PBE can be explained by the high

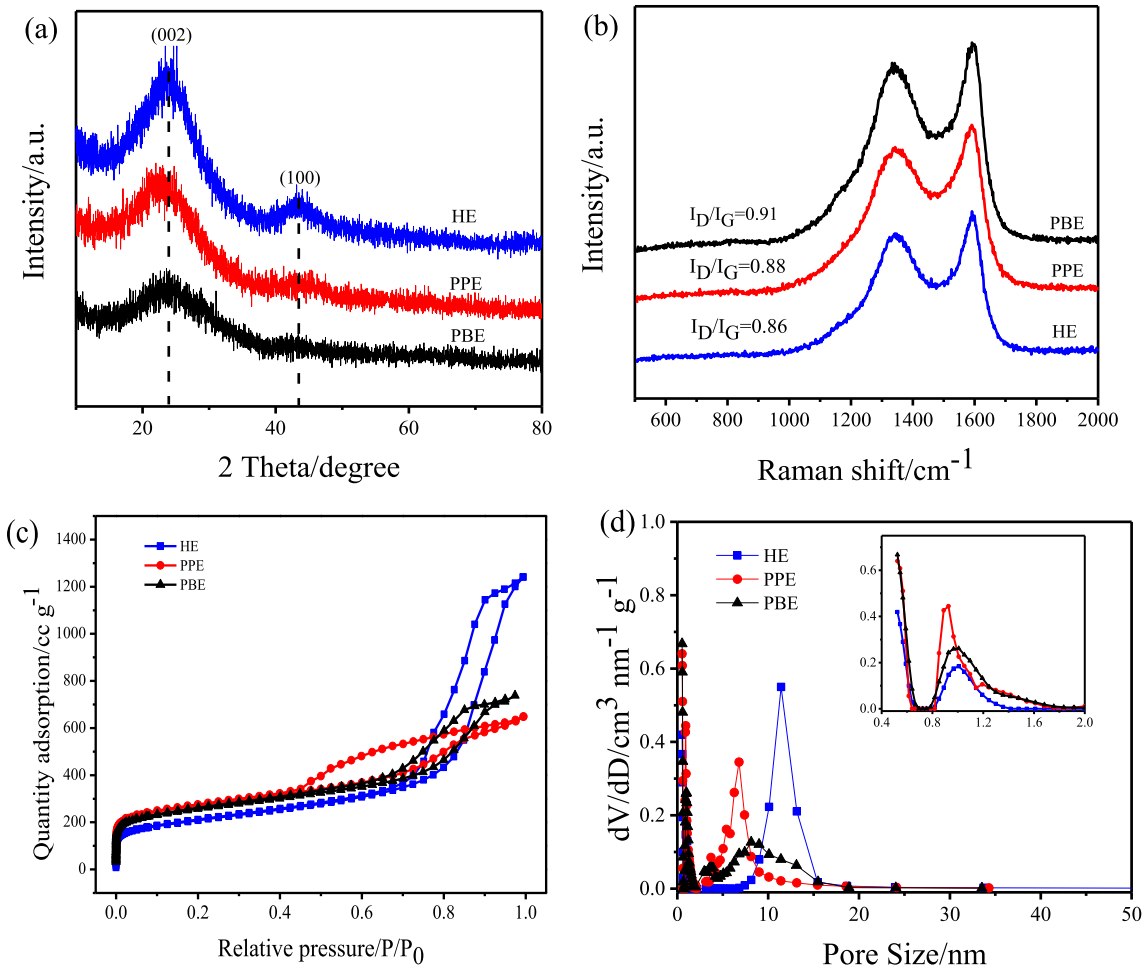

Fig. 4. (a) XRD; (b) Raman spectra; (c) N_2 adsorption–desorption isotherms and (d) pore size distribution of HE, PPE and PBE samples. (A colour version of this figure can be viewed online.)

porosity of the carbon walls in the hierarchically structured PBEs. As can be seen from Fig. 4c, the HE, PPE, and PBE samples exhibit type IV nitrogen adsorption-desorption isotherms, which correspond with the characteristics of mesoporous materials. An obvious hysteresis loop roughly of type H2 at a relative pressure P/P_0 from 0.4 to 1.0 has also been observed in their isotherms, indicating the presence of significant amounts of mesopores [36,37]. Specific surface areas of 1011, 782, and 613 $m^2 g^{-1}$, and mean pore size mainly distributed at 6.5, 8, and 12 nm have been calculated using the Barrett-Joyner-Halenda (BJH) method based on the isotherms for the PPE, PBE, and HE samples, respectively (Fig. 4d). Obviously, the mesosized pores in PPE and PBE (especially for the former) appear smaller in comparison with those of HE. The reduction of mesopore size can be ascribed to the *in-situ* coating of carbon derived from the reaction between C_4F_8 and silica, and an explanation will be discussed in detail below. A steep adsorption slope at relative pressure P/P_0 between 0 and 0.05 can clearly be observed, as well as in the sorption isothermal for these three samples, suggesting the existence of micropores. The density functional theory (DFT) method was used to calculate the pore size distribution of the micropores, which was approximately 0.9 nm for all the samples. The formation of micropores can be ascribed to the *in situ* etching of the carbon precursor by the contained oxygen moieties upon pyrolysis. Such a speculation is confirmed by analyzing the porosity of the as spray-dried chitosan spheres, which show a specific surface area of 57 $m^2 g^{-1}$ and a pore volume of 0.042 cc g^{-1} only (see Fig. S3). Micropore-related specific surface area and pore volume deduced by t-plot analysis are 417 $m^2 g^{-1}$ and 0.186 cc g^{-1} for PBE, respectively, and 470 $m^2 g^{-1}$ and 0.204 cc g^{-1} for PPE, respectively, whereas these values are 234 $m^2 g^{-1}$ and 0.104 cc g^{-1} for HE, respectively, which are smaller than those of PBE and PPE. The low micropore surface area and micropore volume for the HE sample might be due to the reservation of silica nanoparticles during the calcinations. The formation of a stable silica/carbon interface within the SiO_2/carbon spheres will impede the development of micropores by inhibiting the thermal decomposition of surface carbon. The values for the porosity of these samples are listed in Table 2.

From the table one can see that HE sample presents the largest total pore volume (for meso- and micropores). It is reasonable by taking into consideration the large sized mesopores in HE since they could provide higher pore volume than the small sized ones. On the evidence of the SEM measurements, another possible

Table 2
Characteristic surface areas and pore structures of the carbon samples.

Sample	S_{BET} ($m^2 g^{-1}$)		V (cc g^{-1})	
	S_{total}	S_{mico}	V_{total}	V_{mico}
HE	613	234	1.85	0.104
PPE	782	470	1.09	0.204
PBE	1011	417	1.416	0.186

contribution to the high pore volume of HE might come from the slightly larger interparticle spaces among the HE spheres.

3.4. Formation processes and etching mechanism

To illustrate the formation processes and etching mechanism, the structure and composition evolution of the sample during different steps of the etching process were monitored by SEM and examined with EDS. Rod-like PTFE binder with a diameter of approximately 200 nm and spherical PTFE powder with a size of approximately 5 μm were used as silica removal agents and were characterized as depicted in Fig. S4. Interestingly, after the mixing of PTFE binder suspension with silica/chitosan spheres in water and then drying via freeze drying, the silica/chitosan spheres in the obtained solid were densely wrapped with rod-shaped PTFE particles (see Fig. S5). After a thermal treatment, the silica/chitosan composites were covered with PTFE when the solid was heated at 350 °C for a short time (see Fig. S6a and Fig. S7a). When the temperature was increased to 550 °C, the PTFE severely decomposed and macropores formed (Fig. S7d). However, fluorine and silica were detected in both samples (Fig. S6 and Fig. S7), indicating the incomplete removal of silica and partial decomposition of PTFE. When the temperature was increased further to a stage that was much higher than the decomposition point of PTFE, almost no silica and fluorine remained (Fig. S8). Based on the aforementioned experiments and the measurement results, a drawing depicted in Fig. 5 illustrates the derivation of carbon materials with different porosities by controlling the etching strategies. PTFE begins to melt when the thermal treatment temperature reaches its melting point at 327 °C [38]. With the increase of the temperature to above 450 °C, PTFE begins to decompose into gaseous octafluorocyclobutane and tetrafluoroethylene (Eq. (5)).

$$\mathrm{PTFE} \xrightarrow{\Delta} \mathrm{C_nF_x}(\mathrm{C_4F_8}, \mathrm{C_3F_6}, \mathrm{C_2F_4}) \tag{5}$$

$$2\mathrm{F_2C{=}CF_2} \rightarrow \mathrm{gCF_2{-}CF_2{-}CF_2{-}CF_2\cdot} \rightarrow \mathrm{C_4F_8} \tag{6}$$

$$\mathrm{C_4F_8 + 2SiO_2} \rightarrow \mathrm{2SiF_4 + 2CO_2 + 2C} \tag{7}$$

$$\mathrm{C_4F_8 + SiO_2} \rightarrow \mathrm{SiF_4 + 2COF_2 + 2C} \tag{8}$$

$$\text{Polymerization and hydrolysis PTFE} \rightarrow \mathrm{HF} \tag{9}$$

Fig. 5. Schematic illustration of the synthesis processes of porous carbons with different porosity. (A colour version of this figure can be viewed online.)

$$\mathrm{4HF + SiO_2} \rightarrow \mathrm{SiF_4{+}2H_2O} \tag{10}$$

$$\mathrm{3SiF_4 + 2H_2O} \rightarrow \mathrm{2H_2SiF_6 + SiO_2} \tag{11}$$

Due to the lower bond energy of C-C than that of C-F, the former would be the first to break and generate radicals that would then provoke a series of reactions because the formation of tetrafluoroethylene and new radicals is energetically favorable. Furthermore, octafluorocyclobutane can also be derived from two molecules of tetrafluoroethylene via a radical-intermediated annulation reaction (Eq. (6)) [39]. The resulting octafluorocyclobutane can then react with the silica nanoparticles, evoking the silica template etching process (Eq. (7)). The production of silicon tetrafluoride would vaporize, while the carbon materials would deposit *in situ* onto the surfaces of porous carbon spheres. A side reaction between octafluorocyclobutane and silica leads to the production of carbonyl fluoride (Eq. (8)), which would be hydrolyzed to carbon dioxide and give rise to carbon deposition as well [40]. To further verify this speculation, a control experiment using 14-nm-sized silica as a hard template and PTFE powder as an etchant was performed while keeping other experimental conditions constant. Porous carbon with a pore size of approximately 8 nm was obtained, which is obviously smaller than the size of the applied SiO_2 template (see Fig. S9). The discrepancy between the pore size and the size of the applied SiO_2 template (both 12 and 14 nm SiO_2 particles) can be ascribed to the *in-situ* deposition of carbon inside the channels (via Eqs. (7) and (8)), resulting in the reduction of pore size of the derived porous carbon material. Such an assumption has also been proven by the previously described N_2 adsorption-desorption measurements. In addition, hydrofluoric acid generated from the polymerization or hydrolysis of PTFE has been previously documented (Eqs. (9) and (10)) [41] and can also etch silica. However, a high concentration of silicon tetrafluoride derived from the above two etching processes could be adsorbed on the external surface of porous carbon and would then react with water originating from carbonization, resulting in the regrowing of silica particles on the surface (Eq. (11)). The macropores in PBE can be explained by considering the compact contact between the PTFE binder particles and the silica/chitosan spheres. As aforementioned, the rod-like PTFE binder particles are tightly anchored onto the surface of the silica/chitosan spheres after drying. During the one-pot pyrolysis and *in situ* etching process, the PTFE may melt, but it can deposit onto the surface of silica/chitosan spheres and decompose therein. These consecutive processes result in macropores and association with silica etching that leads to the formation of mesopores. For PPE preparation, due to the large size and the lack of dispersibility for PTFE powder, the PTFE powders can simply be mixed with silica/chitosan composites, with no close contact between them. Then, during the following thermal treatment, the PTFE powder may melt but will dislocate from the solid mixture. The dislocated PTFE cannot cause macropores but still can produce mesopores in PPE via gas etching. As control experiments, we tried to modify the etching process by initially separating PTFE binder from its suspension and then mixing it with silica/chitosan spheres, or by dispersing PTFE powder firstly in water to obtain a suspension as that of binder; however, an agglomeration of PTFE binder was obtained during the former attempt, while in the latter case, the PTFE powder was undispersible in water, making it unsuitable for further application (see Fig. S10).

3.5. Electrochemical properties

The electrochemical performances were tested in three-electrode configuration with 6 mol L^{-1} of KOH as the aqueous

electrolyte. Fig. 6a shows the CV curves of these three different porous carbon materials collected at a scan rate of 20 mV s^{-1}. It can be seen that the PBE sample shows the largest current response, demonstrating the best capacitive properties among them. The CV curves of PBE at different scan rates exhibited quasi-rectangle shapes (Fig. 6b), suggesting the superior capacitive behaviors [42]. Additionally, the broadened peak between −0.8 and −0.2 V indicates that the total capacitance mainly originates from the electric double layer capacitance with a contribution of pseudocapacitance raised by oxygen- and nitrogen-related groups on the sample surfaces, as had been confirmed by XPS analysis. The steep slope (close to 90°) of the CV curves also suggests that PBE is highly electrically conductive. A series of GCD tests at different current densities were also conducted for PBE. As shown in Fig. 6c, PBE exhibits the longest discharge time, which is consistent with the CV results. The nearly symmetric and triangular shapes obtained during the GCD tests further demonstrate the rapid current response and excellent electrochemical reversibility. The control experiment shows that the PBE sample with deteriorated structure delivered poor electrochemical performances when it was tested as an electrode material for supercapacitors (see Fig. S2a and Fig. S11), highlighting the importance of structural integrity. The galvanostatic capacitance values of PBE, PPE, and HE, which were determined from the discharge time at a current density of 0.5 A g^{-1}, are 250.5, 213, and 110 F g^{-1}, respectively. Fig. 6d shows the specific capacitance calculated from the GCD profiles at different current densities. It is worth noting that PBE retained 80.5% of its galvanostatic capacitance when the current density increased from 1 to 10 A g^{-1} and showed an outstanding capacitance retention of 65.5% even when the current density soared further to 100 A g^{-1}. The CV curves at various scan rates and GCDs at different current densities for PPE and HE are presented in Fig. S12 for comparison. A comparison of specific capacitance for PBE- and PPE-based supercapacitors with those of other porous carbon materials in documented works has been summarized in Table 3.

Electrochemical impedance spectroscopy (EIS) was employed to further study their electrochemical properties. As shown in Fig. 7a, all the EIS spectra exhibit a small semicircle in the high frequency region and a nearly vertical straight line in the low frequency region, which correspond to charge transfer resistance and Warburg resistance, respectively. Apparently, the almost complete lack of a significant semicircle indicates that PBE has low impedance at the electrode/electrolyte interface and faster ion transportation from the electrolyte to the inner mesopores. From the Bode phase diagrams (Fig. 7b), it can be seen that the phase angle of PBE is approximately 84°, which is close to that of ideal capacitors (90°) and is higher than those of PPE (82°) and HE (78°). The operating frequency and the corresponding characteristic relaxation time constant are an important quantitative index for the reversible charging and discharge speed of the electrode. The PBE sample shows an operating frequency of 1.24 Hz, which is higher than that of PPE (1.16 Hz) and HE (0.765 Hz). The corresponding relaxation time constants of 0.81, 0.87, and 0.99 s, respectively, for the three samples can be derived from the operating frequencies. Therefore, the enhanced ion diffusion of PBE is favorable for rate performance at higher charge-discharge rates. To test the electrochemical stability of PBE, galvanostatic charge/discharge measurements were conducted at a current density of 10 A g^{-1}. As can be seen from

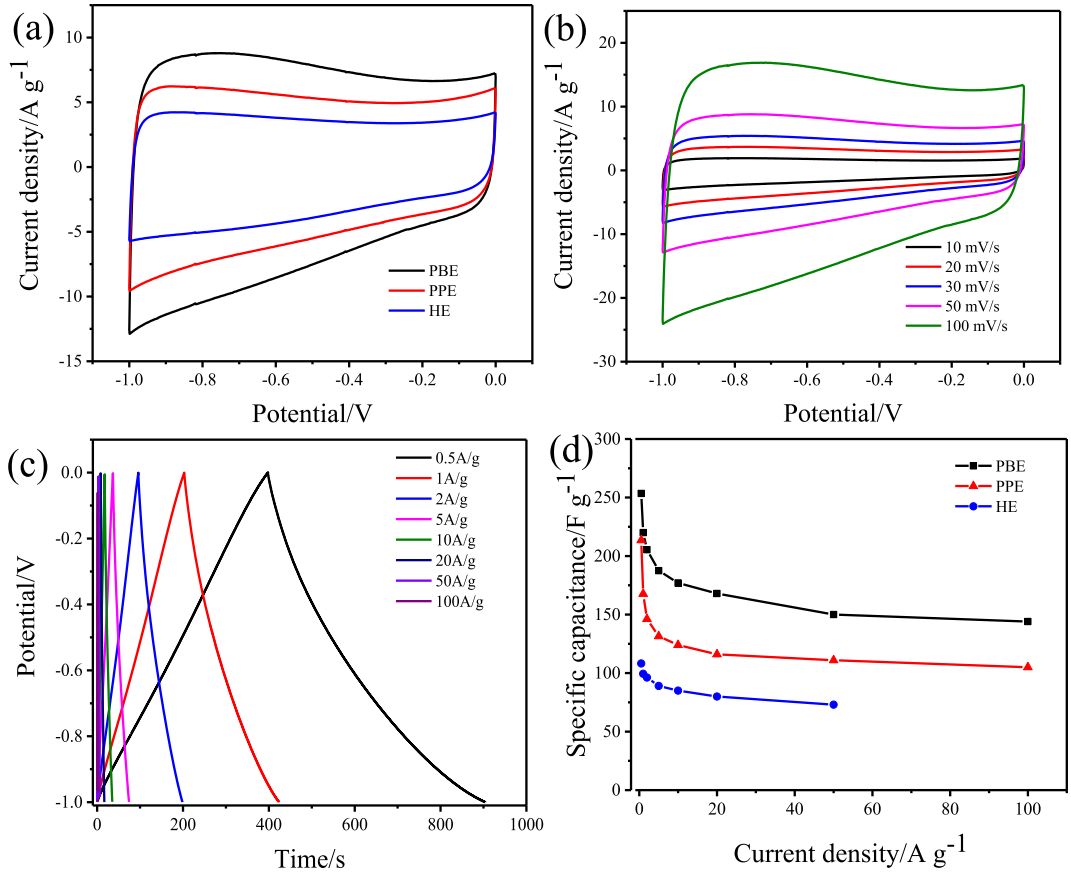

Fig. 6. (a) CV curves of the three samples at 20 mV s^{-1}; (b) CV curves of PBE at different scan rate; (c) GCD curves of PBE; (d) rate performance of electrodes made of these porous carbons with a three-electrode configuration in 6 mol L^{-1} KOH. (A colour version of this figure can be viewed online.)

Table 3
Comparison of the specific capacitance of PBE and PPE with reported carbon materials.

Carbon type	C[a] (F g^{-1})	R[b]	Electrolyte	Ref.
Silica fiber array-templated GTSDC	283	0.25 A g^{-1}	6M KOH	[43]
Hydrogel-derived HHPC	214	0.2 A g^{-1}	6M KOH	[44]
Block copolymer(PS) derived NHPCs	254	0.5 A g^{-1}	6M KOH	[45]
Cotton derived CFs	221.7	0.3 A g^{-1}	6M KOH	[46]
Cattail biomass derived CACs	126.5	0.5 A g^{-1}	6M KOH	[47]
Lignosulphonate-cellulose derived HAPCs	286	0.25 A g^{-1}	6M KOH	[48]
Template-free derived UPCSs	251	1 A g^{-1}	6M KOH	[49]
B, N-codoped chitosan derived 1B-2CHI-WT	227	2 mV s^{-1}	1MH_2SO_4	[50]
Nano-sized silica templated PBE	250.5	0.5 A g^{-1}	6M KOH	This work
PPE	213			

[a] Specific capacitance tested in three-electrode configuration.
[b] Current density or scan rate.

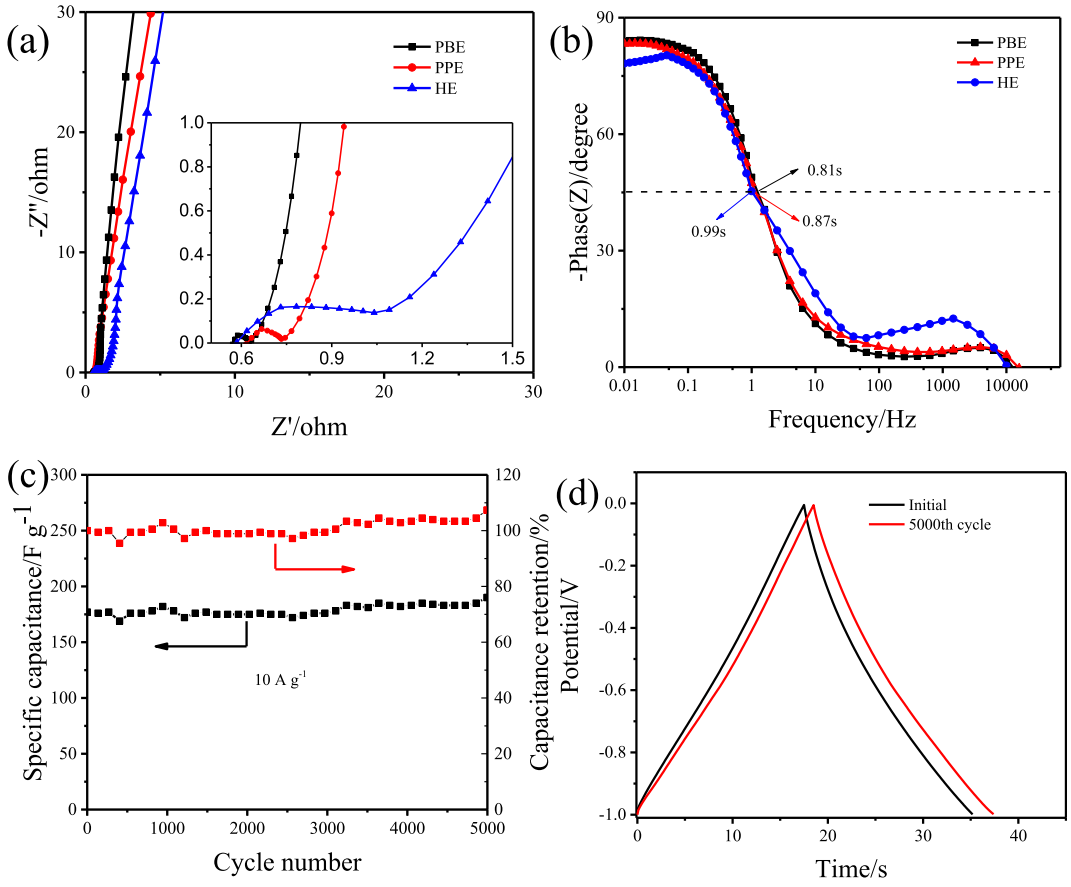

Fig. 7. (a) Nyquist plots (inset: magnification of the Nyquist plot); (b) the frequency response of the as-prepared porous carbon-based supercapacitors in 6 mol L^{-1} KOH; (c) the long-term durability of PBE based electrode;(d) the comparison of GCD lines of the 1st cycle and 5000th cycle. (A colour version of this figure can be viewed online.)

Fig. 7c, the specific capacitance increases even to 190 F g^{-1} after 5000 cycles, which is approximately 107% of the initial capacitance, indicating a highly reversible charge-discharge process and excellent electrochemical reproducibility. Similar improvement of the specific capacitance upon cycling has also been reported for carbon-based electrodes [51,52]. The specific capacitance enhancement usually is attributed to the increase in effective interfacial area between the pores of the electrode material and the electrolyte as the reaction proceeds [53,54]. The same is true for electrodes consisting of PBE, and such a speculation has been proven from the EIS measurement before and after cycles (Fig. S13). Additionally, the GCD curve (Fig. 7d) remains symmetric and triangular in shape and is close to its initial state after cycling, also suggesting high cycling durability. As has been demonstrated with N_2 adsorption-desorption measurements, the PBE sample shows novel hierarchical porosity, in which macro-, meso- and micro-sized pores were intergraded in one system. The high specific capacitance of PBE and PPE samples can be ascribed to their large specific surface area originating mainly from the meso-sized pores and also to the abundance of micropores. The excellent rate capability can be attributed to their unique hierarchical pore structures in which the open macropores can facilitate the diffusion of electrolyte ion in and out of the inferior mesopores. It has already been observed that the capacitive contribution reaches its maximum when the pore size distribution is close to the size of solvated ions of the applied electrolyte or twice that [49]. In the aqueous system,

positively charged ions are presented and thus adsorbed in their hydrated form. All three types of carbon materials possess micropores, with a median pore size of approximately 9 Å, which is larger than that of the dissolved ions ($K^+ \approx H_3O^+ = 3.6–4.2Å > OH^-$) [55]. Therefore, the dissolved ions can be transferred into the micropores less than 1 nm in size, contributing a great portion to the total capacitance. In comparison to HE, PBE and PPE possess larger micropore volume and higher specific surface area. Therefore, they exhibit larger specific capacitance as well. The specific capacitance was enhanced with the increase in micropore volume, demonstrating the contribution of the microsized pores to the capacity as well as the micropore's accessibility to the ions. Additionally, the mesopores can store ions and also facilitate the rapid transport of electrolyte ions to the interior of the bulk material. In contrast to PPE, the PBE sample possesses extra macropores that could shorten the diffusion distance of the ions and act as ion-buffering reservoirs. Additionally, the high content of nitrogen in PBE can not only contribute pseudocapacitance to the total specific capacitance but can also modify the polarity of the carbon matrixes, which will improve the wettability of the carbon matrix and hence enhance the infiltration of ions into the micropores. Clearly, by taking the specific capacity obtained at a current of 0.5 A g^{-1} as a reference, the capacitance retentions for PBE and PPE are 87.8% and 77.5%, respectively, under a current density of 1 A g^{-1}, and 70.8% and 58% at 10 A g^{-1}, suggesting that PBE samples with a hierarchical porous structure are suitable for EDLCs of practical application. According to the equation $E = 1/2CV^2$, the energy density can be impacted by the low operating voltage in aqueous electrolyte, which limits practical application [56]. In order to increase the potential window, we therefore assembled the PBE//PBE-based symmetrical supercapacitor with 1 mol L^{-1} $LiPF_6$ organic solvent as the electrolyte. As shown in Fig. 8a, a typical rectangular CV curve from 0 to 3 V was obtained. The GCD curves at different current densities over the above window potential are presented in Fig. 8b. The cycling stability of the PBE//PBE symmetric supercapacitor was further investigated at a current density of 1 A g^{-1}. After 3000 cycles, the device showed only 14% capacitance decay (Fig. 8c), displaying an excellent long-term cycling durability. The energy density and power density of the device, as shown in a Ragone plot (Fig. 8d), were compared to other potential energy storage devices. The specific energy density of the PBE//PBE device is approximately 28.3 Wh kg^{-1} at a power density of 150.2 W kg^{-1}, and the specific energy density remains at 17.2 Wh kg^{-1} at a high power density of 3000 W kg^{-1}, which is much higher than that of commercial activated carbon (24.8 Wh kg^{-1} at 67.5 W kg^{-1}) [57] and other carbon materials derived from sodium citrate (17 Wh kg^{-1} at 150 W kg^{-1}) [49], polypyrrole (19.5 Wh kg^{-1} at 50 W kg^{-1}) [58], and seaweeds (21.7 Wh kg^{-1}) [59]. Furthermore, by charging for only 2 s at 10 A g^{-1}, two as-fabricated CR2032 coin-type symmetric supercapacitors in series can drive an LED bulb to light for 5 min, which reveals their practical applications in high-rate energy storage.

4. Conclusion

Porous carbon materials with hierarchical porosity or with uniform mesopores were obtained by controlling removal strategies applied to the silica template in the composite microspheres. The solid/gas etching process resulted in silica etching and also *in-*

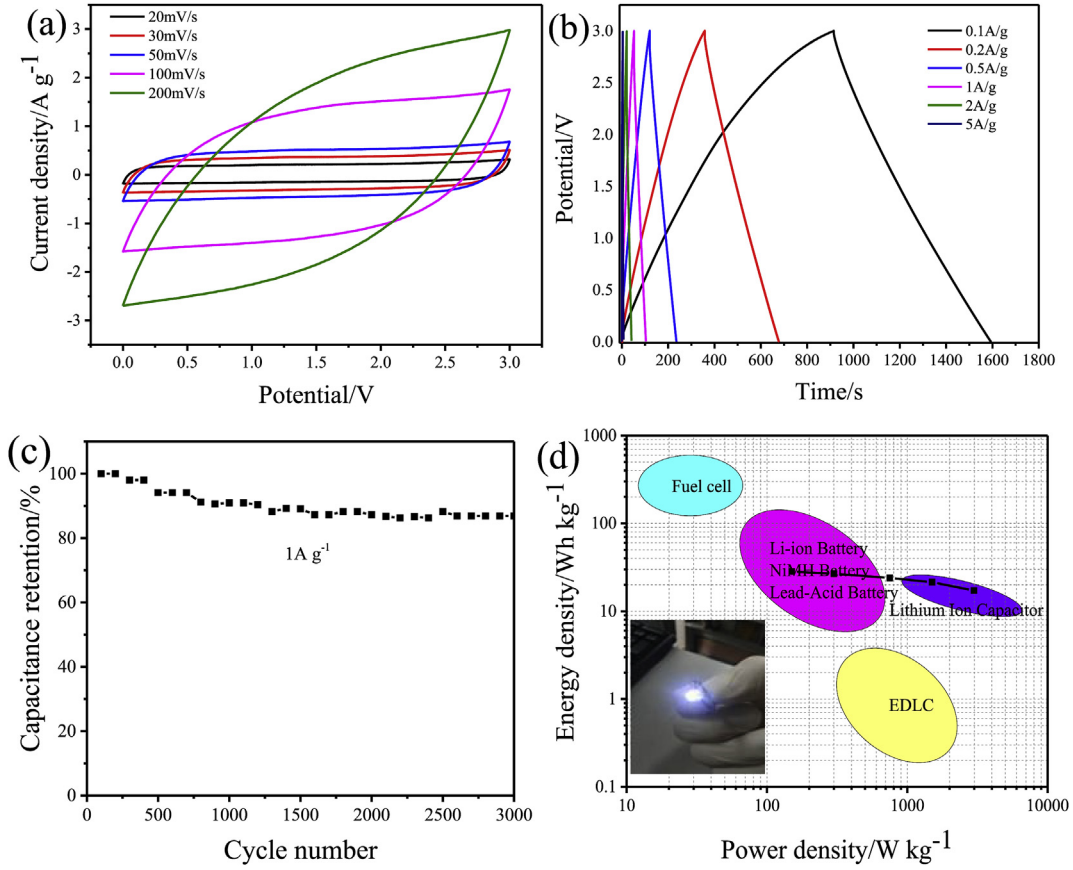

Fig. 8. (a) CV curves; (b) GCD curves; and (c) the long-term durability of PBE based electrode; (d) Ragone plots for the PBE based supercapacitor. (The inset shows two as-fabricated CR2032 coin-type symmetric supercapacitors in series with PBE-based carbon as electrodes can light up a LED bulb brightly.). (A colour version of this figure can be viewed online.)

situ carbon deposition onto the internal walls of the pores. In comparison with PTFE powder and HF aqueous solution, the PTFE binder plays bi-functional roles as etchant and also macropore introduction agent during the one-pot thermal treatment. The approach involving PTFE binder achieves carbonization, template etching, and introduction of additional macropores in one pot, which not only simplifies the fabrication processes but also yields regular honeycomb-like carbon with macro-/meso-/micro-sized hierarchical pores. Porous carbon obtained with PTFE binder as etchant (PBE) exhibits a high specific surface area up to 1011 $m^2 g^{-1}$ and small-sized pores down to 8 nm in comparison with those of 613 $m^2 g^{-1}$ and 12 nm, respectively, for porous carbon derived by HF solution etching (HE). As the electrode material for electrochemical capacitors, PBE exhibits an excellent specific capacitance of 250.5 A g^{-1} at a current density of 0.5 A g^{-1} and a good rate capability with retentions of 80.5% at 10 A g^{-1} and 65.5% even at 100 A g^{-1} in 6 mol L^{-1} KOH aqueous electrolyte. Moreover, a high energy density of 28.3 Wh kg^{-1} and over 86% capacitance retention over 3000 cycles at 1 A g^{-1} were achieved in a symmetric supercapacitor based on PBE in 1 mol L^{-1} $LiPF_6$ organic electrolyte. More importantly, both the spray drying technique and nano-sized silica are available in industry, and chitosan is a type of sustainable biomass, and these ensure the possibility of mass production for this novel porous carbon and reveal the potential for practical application as electrode materials of supercapacitors with superior capacity and durability.

Acknowledgements

This work is supported by the Double First Class University Construction of Shandong Province, the Taishan Scholars Advantageous and Distinctive Discipline Program of Shandong Province for supporting the research team of energy storage materials, and Qingdao Basic & Applied Research Project (15-9-1-56-jch). Y. Q. Wang thanks the financial support from the Top-notch Innovative Talent Program of Qingdao City (Grant no.: 13-CX-8).

Appendix B. Supplementary data

Supplementary data related to this article can be found at https://doi.org/10.1016/j.carbon.2018.01.046.

References

[1] B.E. Conway, Transition from “supercapacitor” to “battery” behavior in electrochemical energy storage, J. Electrochem. Soc. 138 (6) (1991) 1539–1548.
[2] P. Simon, Y. Gogotsi, B. Dunn, Where do batteries end and supercapacitors begin? Science 343 (6176) (2014) 1210–1211.
[3] W. Gu, G. Yushin, Review of nanostructured carbon materials for electrochemical capacitor applications: advantages and limitations of activated carbon, carbide-derived carbon, zeolite-templated carbon, carbon aerogels, carbon nanotubes, onion-like carbon, and graphene, Wires. Energy. Environ 3 (5) (2014) 424–473.
[4] L.L. Zhang, X.S. Zhao, Carbon-based materials as supercapacitor electrodes, Chem. Soc. Rev. 38 (9) (2009) 2520–2531.
[5] A. Vlad, N. Singh, C. Galande, P.M. Ajayan, Design considerations for unconventional electrochemical energy storage architectures, Adv. Energy. Mater. 5 (19) (2015) 1402115.
[6] P. Simon, Y. Gogotsi, Materials for electrochemical capacitors, Nat. Mater. 7 (11) (2008) 845–854.
[7] T. Zhai, L. Wan, S. Sun, Q. Chen, J. Sun, Q. Xia, et al., Phosphate ion functionalized Co_3O_4 ultrathin nanosheets with greatly improved surface reactivity for high performance pseudocapacitors, Adv. Mater. 29 (2017), 1604167.
[8] Y.Q. Zhao, M. Lu, P.Y. Tao, Y.J. Zhang, X.T. Gong, Z. Yang, et al., Hierarchically porous and heteroatom doped carbon derived from tobacco rods for supercapacitors, J. Power Sources 307 (2016) 391–400.
[9] X. Xu, Y. Liu, M. Wang, C. Zhu, T. Lu, R. Zhao, et al., Hierarchical hybrids with microporous carbon spheres decorated three-dimensional graphene frameworks for capacitive applications in supercapacitor and deionization, Electrochim. Acta 193 (2016) 88–95.
[10] C. Liu, Z. Yu, D. Neff, A. Zhamu, B.Z. Jang, Graphene-based supercapacitor with an ultrahigh energy density, Nano Lett. 10 (12) (2010) 4863–4868.
[11] S. Bose, T. Kuila, A. Mishra, R. Rajasekar, N. Kim, J. Lee, Carbon-based nanostructured materials and their composites as supercapacitor electrodes, J. Mater. Chem. 22 (3) (2011) 767–784.
[12] N. Jäckel, M. Rodner, A. Schreiber, J. Jeongwook, M. Zeiger, M. Aslan, et al., Anomalous or regular capacitance? the influence of pore size dispersity on double-layer formation, J. Power Sources 326 (2016) 660–671.
[13] M. Salanne, B. Rotenberg, K. Naoi, K. Kaneko, P.L. Taberna, C.P. Grey, et al., Efficient storage mechanisms for building better supercapacitors, Nat. Energy 1 (6) (2017) 16070.
[14] A. Walcarius, Mesoporous materials and electrochemistry, Chem. Soc. Rev. 42 (9) (2013) 4098–4140.
[15] X.Y. Yang, L.H. Chen, Y. Li, J.C. Rooke, C. Sanchez, B.L. Su, Hierarchically porous materials: synthesis strategies and structure design, Chem. Soc. Rev. 46 (2) (2017) 481–558.
[16] V. Penmatsa, J.H. Yang, Y. Yu, C. Wang, Fabrication of porous carbon micropillars using a block copolymer as porogen, Carbon 48 (14) (2010) 4109–4115.
[17] A. Feng, G. Wu, C. Pan, Y. Wang, The behavior of acid treating carbon fiber and the mechanical properties and thermal conductivity of phenolic resin matrix composites, J. Nanosci. Nanotechnol. 17 (2017) 3786–3791.
[18] C. Luo, S. Niu, G. Zhou, W. Lv, B. Li, F. Kang, et al., Dual-functional hard template directed one-step formation of a hierarchical porous carbon-carbon nanotube hybrid for lithium-sulfur batteries, Chem. Commun. 52 (82) (2016) 12143–12146.
[19] H. Zhao, L. Liu, R. Vellacheri, Y. Lei, Recent advances in designing and fabricating self-supported nanoelectrodes for supercapacitors, Adv. Sci. (2017), 1700188.
[20] D. Wang, A. Fu, H. Li, Y. Wang, P. Guo, J. Liu, et al., Mesoporous carbon spheres with controlled porosity for high-performance lithium–sulfur batteries, J. Power Sources 285 (2015) 469–477.
[21] W. Geng, F. Ma, G. Wu, S. Song, J. Wan, D. Ma, MgO-templated hierarchical porous carbon sheets derived from coal tar pitch for supercapacitors, Electrochim. Acta 191 (2016) 854–863.
[22] D.W. Wang, F. Li, M. Liu, G.Q. Lu, H.M. Cheng, 3D aperiodic hierarchical porous graphitic carbon material for high-rate electrochemical capacitive energy storage, Angew. Chem. 120 (2008) 379–382.
[23] G. Wu, Y. Cheng, Z. Yang, Z. Jia, H. Wu, L. Yang, et al., Design of carbon sphere/magnetic quantum dots with tunable phase compositions and boost dielectric loss behavior, Chem. Eng. J. 333 (2018) 519–528.
[24] X. Liu, M. Antonietti, Molten salt activation for synthesis of porous carbon nanostructures and carbon sheets, Carbon 69 (2) (2014) 460–466.
[25] Z. Yu, X. Wang, X. Song, Y. Liu, J. Qiu, Molten salt synthesis of nitrogen-doped porous carbons for hydrogen sulfide adsorptive removal, Carbon 95 (2015) 852–860.
[26] S.H. Wu, C.Y. Mou, H.P. Lin, Synthesis of mesoporous silica nanoparticles, Chem. Soc. Rev. 42 (9) (2013) 3862–3875.
[27] H. Wang, K. Huang, P. Wang, J. Zhong, Synthesizing nitrogen-doped porous carbon@sulfur cathode for high-performance and stable cycling Li-S batteries, J. Alloy. Comp. 691 (2017) 613–618.
[28] S. Han, T. Hyeon, Simple silica-particle template synthesis of mesoporous carbons, Chem. Commun. 19 (19) (1999) 1955–1956.
[29] Y. Wang, A. Fu, X. Liu, Y. Wang, Y. Li, P. Guo, et al., Porous carbon directed growth of carbon modified MnO_2 porous spheres for pseudocapacitor applications, J. Alloy. Comp. 717 (2017) 341–349.
[30] W. Porcham, Process for Producing Silicon Tetrafluoride, 1986. US, US 4615872 A.
[31] L.L. Zhang, X. Zhao, H. Ji, M.D. Stoller, L. Lai, S. Murali, et al., Nitrogen doping of graphene and its effect on quantum capacitance, and a new insight on the enhanced capacitance of N-doped carbon, Energy Environ. Sci. 5 (11) (2012) 9618–9625.
[32] F. Su, C.K. Poh, J.S. Chen, G. Xu, D. Wang, Q. Li, et al., Nitrogen-containing microporous carbon nanospheres with improved capacitive properties, Energy Environ. Sci. 4 (3) (2011) 717–724.
[33] A. Kajdos, A. Kvit, F. Jones, J. Jagiello, G. Yushin, Tailoring the pore alignment for rapid ion transport in microporous carbons, J. Am. Chem. Soc. 132 (10) (2010) 3252–3253.
[34] Q. Wang, J. Yan, Y. Wang, G. Ning, Z. Fan, T. Wei, et al., Template synthesis of hollow carbon spheres anchored on carbon nanotubes for high rate performance supercapacitors, Carbon 52 (2) (2013) 209–218.
[35] J. Zhang, J. Jiang, H. Li, X.S. Zhao, A high-performance asymmetric supercapacitor fabricated with graphene-based electrodes, Energy Environ. Sci. 4 (10) (2011) 4009–4015.
[36] H. Li, H. Liu, A. Fu, G. Wu, M. Xu, G. Pang, et al., Synthesis and characterization of N-doped porous TiO_2 hollow spheres and their photocatalytic and optical properties, Materials 9 (2016) 849.
[37] M. Kruk, M. Jaroniec, Gas adsorption characterization of ordered organic–inorganic nanocomposite materials, Chem. Mater. 13 (10) (2001) 3169–3183.
[38] Y.P. Khanna, The melting temperature of polytetrafluoroethylene, J. Mater. Sci. Lett. 7 (8) (1988) 817–818.
[39] C.M. Simon, W. Kaminsky, Chemical recycling of polytetrafluoroethylene by pyrolysis, Polym. Degrad. Stabil. 62 (1) (1998) 1–7.
[40] J.N. Butler, The thermal decomposition of octafluorocyclobutane, J. Am. Chem. Soc. 84 (8) (1962) 1393–1398.

[41] D.K. Singh, K.S. Krishna, S. Harish, S. Sampath, M. Eswaramoorthy, No more HF: teflon-assisted ultrafast removal of silica to generate high-surface-area mesostructured carbon for enhanced CO_2 capture and supercapacitor performance, Angew. Chem. Int. Ed. 55 (6) (2016) 2032–2036.
[42] C.C. Hu, C.C. Wang, Effects of electrolytes and electrochemical pretreatments on the capacitive characteristics of activated carbon fabrics for supercapacitors, J. Power Sources 125 (2) (2004) 299–308.
[43] D. Jia, X. Yu, H. Tan, X. Li, F. Han, L. Li, et al., Hierarchical porous carbon with ordered straight micro-channels templated by continuous filament glass fiber array for high performance supercapacitor, J. Mater. Chem. 5 (4) (2017) 1516–1525.
[44] B. You, F. Kang, P. Yin, Q. Zhang, Hydrogel-derived heteroatom-doped porous carbon networks for supercapacitor and electrocatalytic oxygen reduction, Carbon 103 (2016) 9–15.
[45] Y.X. Tong, X.M. Li, L.J. Xie, F.Y. Su, J.P. Li, G.H. Sun, et al., Nitrogen-doped hierarchical porous carbon derived from block copolymer for supercapacitor, Energy Storage Mater. 3 (2016) 140–148.
[46] Y. Liu, Z. Shi, Y. Gao, W. An, Z. Cao, J. Liu, Biomass-swelling assisted synthesis of hierarchical porous carbon fibers for supercapacitor electrodes, ACS Appl. Mater. Interfaces 8 (42) (2016) 28283–28290.
[47] M. Yu, Y. Han, J. Li, L. Wang, CO_2-activated porous carbon derived from cattail biomass for removal of malachite green dye and application as supercapacitors, Chem. Eng. J. 317 (2017) 493–502.
[48] Z. Zhao, S. Hao, P. Hao, Y. Sang, A. Manivannan, N. Wu, et al., Lignosulphonate-cellulose derived porous activated carbon for supercapacitor electrode, J. Mater. Chem. 3 (29) (2015) 15049–15056.
[49] W. Yang, W. Yang, F. Ding, L. Sang, Z. Ma, G. Shao, Template-free synthesis of ultrathin porous carbon shell with excellent conductivity for high-rate supercapacitors, Carbon 111 (2017) 419–427.
[50] Z. Ling, G. Wang, M. Zhang, X. Fan, C. Yu, J. Yang, et al., Boric acid-mediated B, N-co-doped chitosan-derived porous carbons with a high surface area and greatly improved supercapacitor performance, Nanoscale 7 (12) (2015) 5120–5125.
[51] J. Yan, J. Liu, Z. Fan, T. Wei, L. Zhang, High-performance supercapacitor electrodes based on highly corrugated graphene sheets, Carbon 50 (6) (2012) 2179–2188.
[52] Y. Zhang, G. Wen, P. Gao, S. Bi, X. Tang, D. Wang, High-performance supercapacitor of macroscopic graphene hydrogels by partial reduction and nitrogen doping of graphene oxide, Electrochim. Acta 221 (2016) 167–176.
[53] M. Beidaghi, C. Wang, Micro-supercapacitors based on interdigital electrodes of reduced graphene oxide and carbon nanotube composites with ultrahigh power handling performance, Adv. Funct. Mater. 22 (21) (2012) 4501–4510.
[54] Y. Yoon, K. Lee, C. Baik, H. Yoo, M. Min, Y. Park, et al., Anti-solvent derived non-stacked reduced graphene oxide for high performance supercapacitors, Adv. Mater. 25 (32) (2013) 4437–4444.
[55] D. Hulicova, M. Kodama, H. Hatori, Electrochemical performance of nitrogen-enriched carbons in aqueous and non-aqueous supercapacitors, Chem. Mater. 18 (9) (2006) 2318–2326.
[56] N. Jabeen, A. Hussain, Q. Xia, S. Sun, J. Zhu, H. Xia, High-performance 2.6 V aqueous asymmetric supercapacitors based on in situ formed $Na_{0.5}MnO_2$ nanosheet assembled nanowall arrays, Adv. Mater. 29 (2017), 1700804.
[57] Y. Liang, F. Liang, H. Zhong, Z. Li, R. Fu, D. Wu, An advanced carbonaceous porous network for high-performance organic electrolyte supercapacitors, J. Mater. Chem. 1 (24) (2013) 7000–7005.
[58] G.A. Ferrero, A.B. Fuertes, M. Sevilla, N-doped porous carbon capsules with tunable porosity for high-performance supercapacitors, J. Mater. Chem. 3 (6) (2015) 2914–2923.
[59] E. Raymundo-Piñero, M. Cadek, F. Béguin, Tuning carbon materials for supercapacitors by direct pyrolysis of seaweeds, Adv. Funct. Mater. 19 (7) (2009) 1032–1039.